Characterizing and Overcoming Spectral Artifacts in Imaging Fourier-Transform Spectroscopy of Turbulent Exhaust Plumes

Elizabeth A. Moore[1], Kevin C. Gross[1*], Spencer J. Bowen[1], Glen P. Perram[1], Martin Chamberland[2], Vincent Farley[2*], Jean-Philippe Gagnon[2], Philippe Lagueux[2], André Villemaire[2]
[1]Air Force Institute of Technology, Dept. of Engineering Physics, Wright-Patterson AFB, OH 45433
[2]Telops, Inc., 100-2600 St-Jean-Baptiste, Quebec, Qc, G2E 6J5, Canada

ABSTRACT

The midwave and shortwave infrared regions of the electromagnetic spectrum contain rich information enabling the characterization of hot, rapid events such as explosions, engine plumes, flares and other combustion events. High-speed sensors are required to analyze the content of such rapidly evolving targets. Cameras with high frame rates and non-imaging spectrometers with high data rates are typically used; however the information from these two types of instruments must be later fused to enable characterization of the transient targets. Imaging spectrometers have recently become commercially available for general scientific use, thus enabling simultaneous capture of both spatial and spectral information without co-registration issues. However, their use against rapidly-varying sources has traditionally been considered problematic, for even at moderate spatial and spectral resolutions the time to acquire a single spectrum can be long compared to the timescales associated with combustion events.

This paper demonstrates that imaging Fourier-transform spectroscopy (IFTS) can successfully characterize the turbulent combustion exhaust from a turbojet engine. A Telops Hyper-Cam IFTS collected hyperspectral video from a Turbine Technologies SR-30 turbojet engine with a spectral resolution of $\delta\tilde{\nu} = 1$ cm^{-1} on a 200×64 pixel sub-window at a rate of 0.3 Hz. Scene-change artifacts (SCAs) are present in the spectra; however, the stochastic fluctuations in source intensity translate into high-frequency "noise." Temporal averaging affords a significant reduction of the noise associated with SCAs. Emission from CO and CO_2 are clearly recognized in the averaged spectra, and information about their temperature and relative concentrations is evident.

Keywords: imaging spectroscopy, FTS, jet engine exhaust, turbulence, scene-change artifacts, source noise

1. INTRODUCTION

With the development of the digital computer and the Cooley-Tukey algorithm for computing numerical Fourier-transforms, spectrometers based on interferometry have become ubiquitous, particularly for studies in the infrared portion of the electromagnetic spectrum. Well-known advantages of Fourier-transform spectrometers (FTS) over other spectral measurement techniques include the Jacquinot advantage (high throughput through a circular aperture instead of a slit), the Felgett advantage (measurement of all wavelengths simultaneously), and the Connes advantage (superior accuracy of the frequency axis).[1,2] Recent advances in electronics and focal-plane array (FPA) technologies have enabled the development of imaging Fourier-transform spectrometers (IFTS).

While there are several advantages to interferometric spectroscopy, a primary disadvantage is the sensitivity the instrument has to source intensity fluctuations. Variations in source intensity during the collection of an interferogram will result in artifacts in the Fourier-transformed spectrum. These scene-change artifacts (SCA) have received only limited discussion in the literature[3-5], and most practicing spectroscopists using FTS ensure that the source under study is static. It is well understood that to study an evolving source, the measurement timescale must be much shorter than the timescale associated with the intensity variations. Kick *et al.* recently treated from a theoretical perspective the effects of a source intensity that varies linearly or quadratically in time on the spectrum obtained via FTS.[4] Mitchell *et al.* performed field measurements to illustrate the negative effect of platform jitter on measured spectra.[5] In light of this discussion, it might

* Further author information
KCG: kevin.gross@afit.edu, +1 (937) 255-3636 x4558
VF: vincent.farley@telops.com, +1 (418) 864-7808 x481

Report Documentation Page

Form Approved
OMB No. 0704-0188

1. REPORT DATE	2. REPORT TYPE	3. DATES COVERED
OCT 2009	**N/A**	**-**

4. TITLE AND SUBTITLE	5a. CONTRACT NUMBER
Characterizing and Overcoming Spectral Artifacts in imaging Fourier transform Spectroscopy of Turbulent Exhaust Plumes	5b. GRANT NUMBER
	5c. PROGRAM ELEMENT NUMBER
6. AUTHOR(S)	5d. PROJECT NUMBER
	5e. TASK NUMBER
	5f. WORK UNIT NUMBER
7. PERFORMING ORGANIZATION NAME(S) AND ADDRESS(ES) **AFIT WPAFB, OH 45433**	8. PERFORMING ORGANIZATION REPORT NUMBER
9. SPONSORING/MONITORING AGENCY NAME(S) AND ADDRESS(ES)	10. SPONSOR/MONITOR'S ACRONYM(S)
	11. SPONSOR/MONITOR'S REPORT NUMBER(S)

12. DISTRIBUTION/AVAILABILITY STATEMENT
Approved for public release, distribution unlimited

13. SUPPLEMENTARY NOTES
See also ADB381583. RTO-MP-SET-151 Thermal Hyperspectral Imagery (Imagerie hyperspectrale thermique). Meeting Proceedings of Sensors and Electronics Panel (SET) Specialists Meeting held at the Belgian Royal Military Academy, Brussels, Belgium on 26-27 October 2009., The original document contains color images.

14. ABSTRACT

15. SUBJECT TERMS

16. SECURITY CLASSIFICATION OF:			17. LIMITATION OF ABSTRACT	18. NUMBER OF PAGES	19a. NAME OF RESPONSIBLE PERSON
a. REPORT	b. ABSTRACT	c. THIS PAGE			
unclassified	**unclassified**	**unclassified**	**SAR**	**12**	

Standard Form 298 (Rev. 8-98)
Prescribed by ANSI Std Z39-18

seem that FTS cannot be applied to the study of transient combustion events. However, our group has demonstrated that rapidly evolving combustion fireballs from high explosives can be studied using modern non-imaging FTS instruments capable of operating between 10–100 Hz.[6-9]

Non-imaging FTS has been successfully applied to the study of exhaust from commercial aircraft jet engines.[10-12] CO, CO_2, NO_x, and unburned hydrocarbons can be detected and correlated with engine performance. Imaging spectroscopy of jet engines has even been accomplished using a FTS with an azimuth/elevation mirror to form a raster-based hyperspectral image.[13-14] The primary purpose of the raster-based spectral imaging is to locate and track the single pixel representing the brightest region of the exhaust plume. In the reported non-imaging and raster-based imaging spectral measurements, the field-of-view (FOV) at the plume was on the order of 10–100 cm in diameter.

Measurements of jet engine exhaust plumes at both high spectral and high spatial resolutions could be useful in several contexts. For example, some retrieval algorithms developed to interpret non-imaging FTS measurements of aircraft exhaust assume an axisymmetric plume.[11] High spatial resolution measurements can identify deviation from this assumption as well as provide additional information to determine the actual distribution of temperatures and concentrations throughout the plume. High fidelity hyperspectral spectral measurements could also be used to benchmark computational fluid dynamic simulations of turbulent flow fields from jet engines. While such benchmarking has been performed, the spatial and spectral resolutions that can be achieved with IFTS would provide an unprecedented level of detail for comparison. To begin this research effort, measurements were made recently on an education-class turbojet engine using a Telops Hyper-Cam midwave infrared (MWIR) hyperspectral camera, which is based on a Michelson interferometer. A consequence of the narrow instantaneous FOV is that the turbulent fluctuations in the exhaust plume cause large, stochastic variations in pixel intensity during the acquisition of interferograms. The associated SCAs in the spectra are significant. The purpose of this paper is two-fold: (1) to empirically demonstrate that SCAs can be minimized via temporal averaging, and (2) to discuss how the turbulence affects the measured spectra.

2. EXPERIMENTAL

2.1 Imaging Spectrometer Description

The Hyper-Cam-MWE-Fast, like the other members of the Hyper-Cam family (LW, MW and MWE), is a lightweight and compact imaging radiometric spectrometer. This field-portable sensor is shown in Figure 1. The spectral measurements are performed using a Fourier-transform spectrometer. It uses a 320×256 MWIR InSb focal plane array detector that can

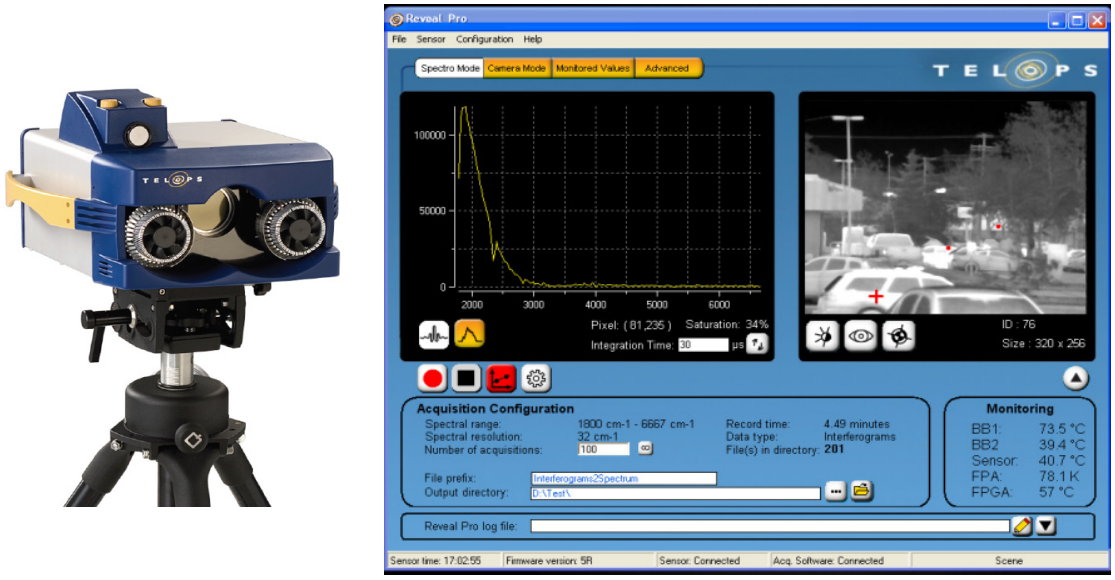

Fig. 1. Picture of the Hyper-Cam-MWE-Fast sensor (left) and screenshot of the Reveal Pro software (right) that gives the operator real-time feedback, including the broadband IR image and the spectrum of a selected pixel.

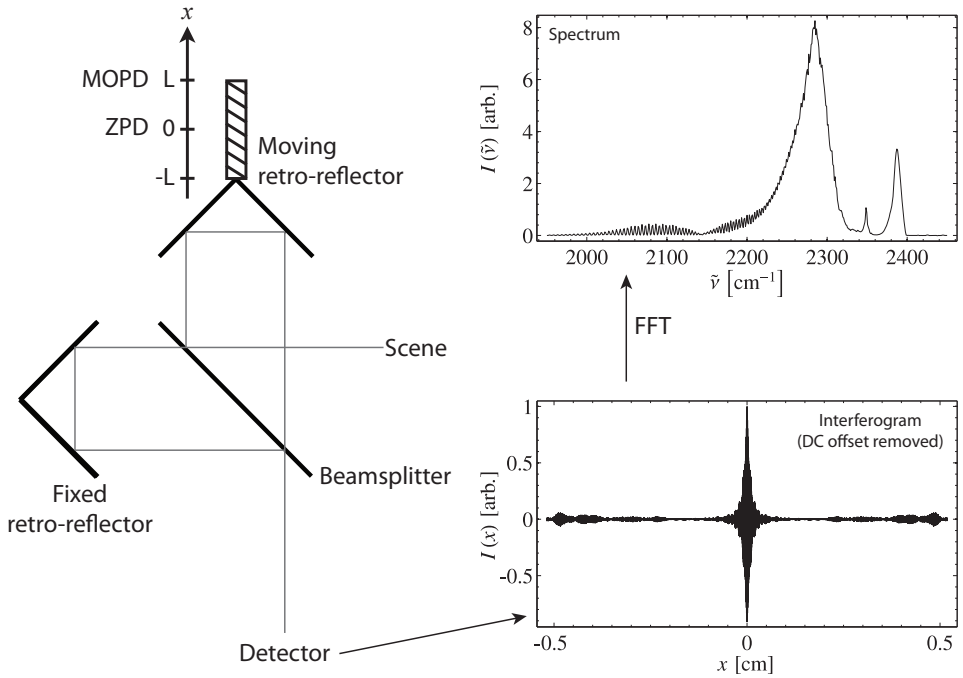

Fig. 2. A simplified schematic of the Michelson interferometer inside the Telops Hyper-Cam. The detector is a 320×256 InSb focal plane array. An interferogram cube is generated by acquiring broadband images at each mirror position x. The interferogram at each pixel contains the DC offset. For a static scene, the DC offset is easily removed and a numerical Fourier transform produces the corresponding spectrum.

be windowed and formatted to fit the desired size and to decrease the acquisition time. Spectral resolution is user selectable and ranges from 0.25 to 150 cm^{-1}. This instrument generates a complete spectrum of each pixel in the image. Each pixel has an instantaneous field-of-view (IFOV) of 0.35 mrad providing an overall FOV of 112×90 mrad. Higher spatial resolution (IFOV of 100 µrad) is possible with the addition of a reflective telescope. The sensor can focus IR images from a distance of 3 meters up to infinity. Reveal Pro provides a user-friendly interface to the hyperspectral sensor as well as to provide real-time feedback to the operator (refer to Figure 1). Within the Spectro Mode, the non-uniformity corrected broadband IR image is displayed in real-time. Moreover, the raw spectrum or interferogram (user chosen) of a user selected pixel in the IR image is also displayed in real-time.

The Hyper-Cam-MWE-Fast covers the spectral range from 1.5 µm to 5.5 µm (1800–6667 cm^{-1}). The spectral band and acquisition rates provided by the Hyper-Cam-MWE make it ideal for the study combustion events such as explosions and jet engine combustion. The instrument noise-equivalent spectral radiance (NESR) is approximately 10 $nW/cm^2/sr/cm^{-1}$ per pixel at 5 µm for a single measurement at 32 cm^{-1} spectral resolution.

The FPA has a 14-bit dynamic range which can be optimally filled by selection of an integration time between 5 µs–15 ms. A 16-tap read-out integrated circuit enables camera frame rates exceeding 1200 Hz, and sub-windowing is possible enabling higher frame rates at a reduced FOV. The sensor also has advanced acquisition and processing electronics, including 4 GB of high-speed DDR-SRAM, with the capability to convert the raw interferograms into raw spectra using real-time Discrete-Fourier Transform (DFT). Moreover, co-adding and spectral cropping can be performed real-time with onboard processing electronics capable of data rates exceeding 150 Mpixels/s.[15] The Hyper-Cam family was presented in detail in previous papers.[16-17]

The instrument is a Michelson-type interferometer, and a simplified schematic is presented in Figure 2. Interferogram datacubes are formed by capturing broadband images at various mirror positions or optical path differences (OPDs). Thus, unlike most non-imaging FTS systems, the DC-level is not filtered out electronically. Hyperspectral images are formed by Fourier-transforming the interferograms at each pixel. The spectral resolution $\delta\tilde{\nu}$ of the hyperspectral images is defined by the maximum optical path difference (MOPD) via $\delta\tilde{\nu} = 0.6\times MOPD^{-1}$. The rate at which hyperspectral imag-

Table 1. The dependence of camera frame rate and hyperspectral imagery acquisition rate on FPA window size, FPA integration time, and spectral resolution. The last two rows correspond to the instrument configurations used on the two jet engine field measurements.

Window size	Integration time [μs]	MOPD / Spectral Resolution [cm] / [cm^{-1}]	Camera Rate / # of OPDs [Hz] / #	Hyperspectral Data Rate [Hz]
320×256	10	0.15 / 4	355 / 4741	0.075
320×256	100	0.25 / 4	226 / 4741	0.047
64×32	10	0.019 / 32	17,300 / 593	25
128×128	7	0.038 / 16	4815 / 1185	3.9
64×200	50	0.6 / 1	4780 / 18,963	0.24

ery is captured depends on the FPA window size, integration time, mirror sweep speed, and spectral resolution. Table 1 lists the acquisition rate for hyperspectral imagery at several different instrument configurations. A two-point instrument calibration to radiance [W/cm^2/sr/cm^{-1}] can be accomplished by using the two on-board blackbody sources which overfill the instrument's FOV. One blackbody can reach 100°C and the other features active cooling to enable temperature measurements from 10°C below-ambient up to 40°C.

2.2 Jet Engine Measurements

The exhaust plume from a Turbine Technologies SR-30 turbojet[18] was studied to investigate the degree to which turbulent intensity fluctuations would corrupt spectral measurements by IFTS. The SR-30 is a small turbojet designed for educational laboratory work. A single-stage centrifugal compressor operating between 39,000–87,000 rpm delivers air to the 27 cm long × 17 cm diameter engine designed for combusting various fuels including Jet-A, JP-8, diesel, and kerosene. Maximum thrust of the SR-30 is approximately 178 N with a nominal exhaust temperature of 720 °C.

A set of field measurements was made on the exhaust plume from the SR-30 in November 2008. A brief overview of the test setup is presented; additional details can be found in Bowen's thesis[19]. The SR-30 was set up approximately 11 m from the Telops IFTS and oriented so that the plume was perpendicular to the IFTS. A matte-black surface was placed behind the jet engine to provide a uniform background scene. Hyperspectral image cubes were collected on a 200×64 pixel sub-window with a spectral resolution of $\delta\tilde{\nu}$ = 1 cm^{-1} at a rate of approximately 0.3 Hz. This field of view corresponded to 73×23 cm^2 with each pixel covering 0.36×0.36 cm^2. To prevent saturation of the FPA, a custom variable iris was fabricated and placed at the aperture stop of the instrument. With the iris in place, an integration time of 50 μs was used. Measurements of the SR-30 exhaust plume were made with the engine running on kerosene or diesel fuel. For each fuel, measurements were taken at engine speeds of 59,800 and 78,600 RPM corresponding to fuel flow rates of 225 and 300 cm^3/min, respectively. The engine was run for several minutes at the specified RMP and fuel flow rate to achieve stable, steady-state performance. Then approximately 200 individual interferogram cubes were collected. This process was repeated for each of the four test configurations. Calibration data was collected against the internal blackbodies set to 20 and 80 °C before and after each set of 200 measurements. Note that only raw uncalibrated spectra are presented in this work. A rake of six K-type thermocouples was placed into the plume to measure the exhaust temperature. Pictures of the experimental setup are provided in Figure 3.

Spectral measurements were also made by a non-imaging ABB-Bomem MR-254 FTS co-located with the Telops IFTS. The MR-254 collected approximately 4000 time-resolved spectra at 0.6 cm^{-1} resolution with an InSb detector during the time the Telops collected its 200 scans for each specific fuel/RPM engine configuration. The angular FOV was 28 mrad providing a 31 cm diameter circular FOV at the plume. The ABB-Bomem FTS was aligned to capture only the plume; emission and solar reflection from the engine body were outside of the instrument's FOV.

3. RESULTS

Figure 4 presents a summary view of the collection of a single hyperspectral image from the turbulent exhaust plume exiting the SR-30 turbojet engine while burning diesel fuel and operating at 78,600 RPM. The top panel image shows

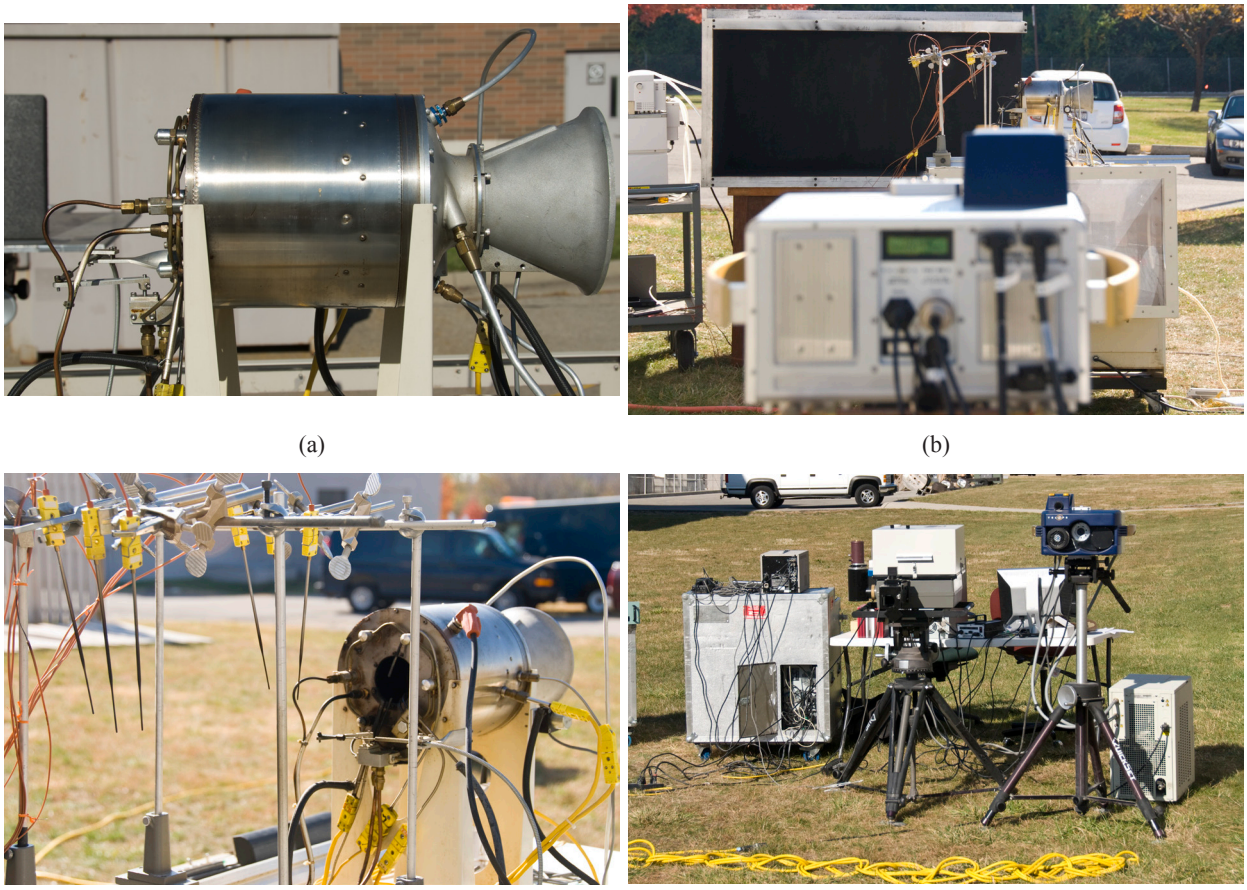

(a) (b)

(c) (d)

Fig. 3. (a) Close-up of the Turbine Technologies SR-30 turbojet. Air enters from the right and hot exhaust exits on the left. (b) The engine on the test stand against a uniform, black background. A rake of thermocouples is visible to the left of the engine. (c) The exit port of the engine is shown, and the thermocouples are visible. (d) The ABB/Bomem MR-254 FTS (left) and Telops Hyper-Cam IFTS (right).

the intensity data collected at the first OPD. The intensities have been normalized by the FPA dynamic range (2^{14}) and the values are between 0.3–0.95. To improve visualization of the plume, the color range is limited to 0.325–0.7 and the image has been cropped to 128×32 pixels. Solar reflection off of the engine dominates the signal and is responsible for the irregularly-shaped bright spot centered near pixel (105, 20). The plume originates near pixel (105, 16) and travels to the left. The appearance of a vertical checkerboard pattern near pixel columns 73 and 45 are due to the support structure holding the thermocouple probes in place.

The second panel of Figure 4 illustrates the difference in brightness between images taken at the first and second OPD. A small portion of the variation in brightness is due to the change in the interference pattern which accompanies a change in the OPD. However, this variation is imperceptible compared to the large variations in brightness due to turbulence. The swirling turbulent eddies are evident as round or oval-like regions in the difference image. Subsequent difference images (not shown) reveal the temporal evolution of these eddies as they break up while traveling down the plume, in addition to the creation of new turbulent vortices at engine aft.

Two pixels from the interferogram cube are presented in the bottom-left panel of Figure 4 and correspond to the indicated regions in the top panel. The interferogram $I(x)$ of pixel 1 corresponds to a point near the exhaust port of the engine where the turbulence is large. A second pixel far down stream is also shown for comparison. Both interferograms are peak-normalized and pixel 2's interferogram has been vertically and horizontally offset to improve visualization. Both interferograms appear highly noisy as a result of the rapid, stochastic intensity fluctuations caused by the turbulence in

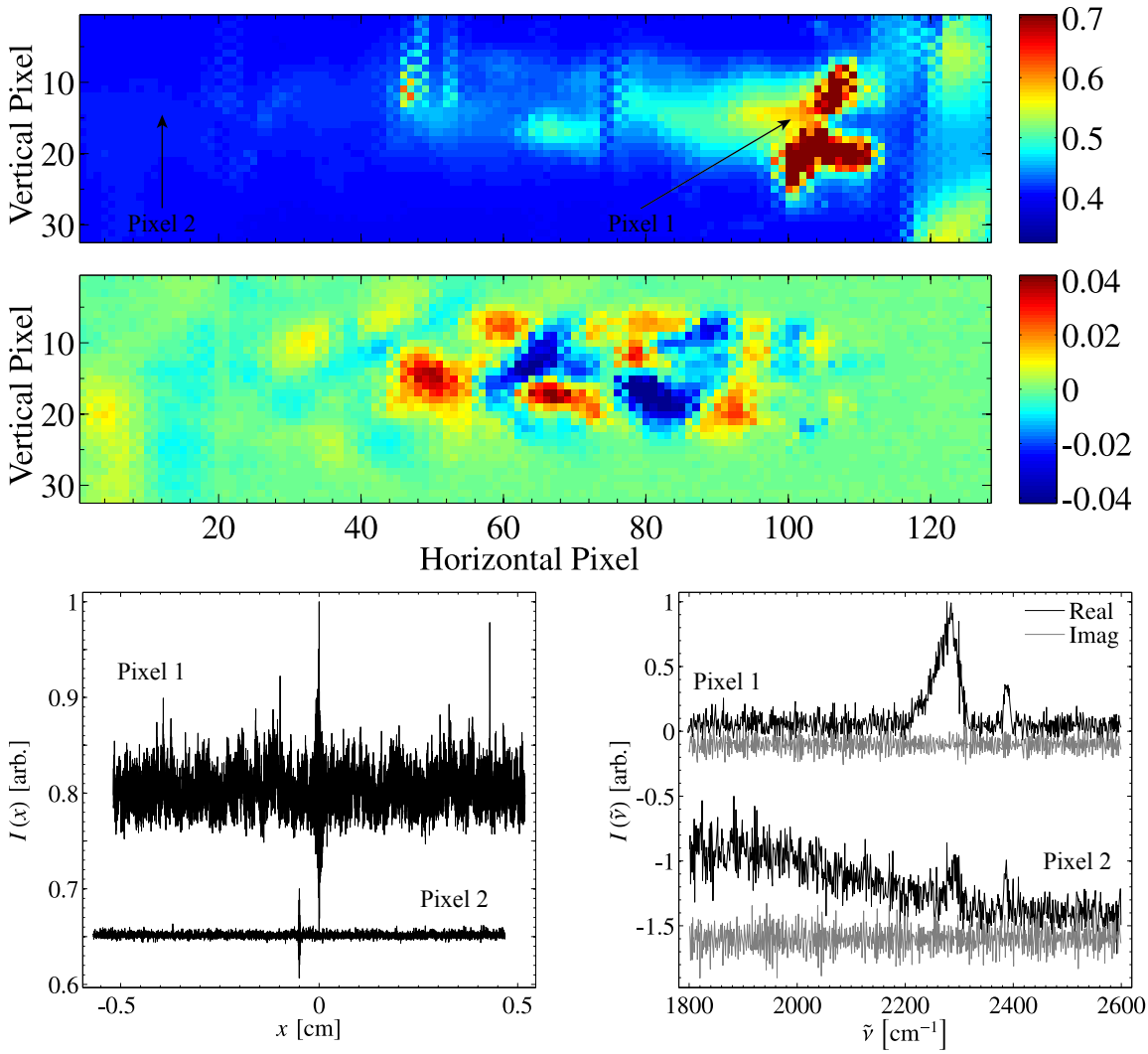

Fig. 4. *Top panel*: Broadband image of the turbojet plume at the first OPD. *Middle panel*: Difference between the first and second broadband images reveal the turbulent eddies and their effect on the DC component of the interferogram. By comparison, intensity variations caused by modulation due to the difference in mirror position are small. *Bottom-left panel*: The interferograms corresponding to pixel 1 and 2 (as indicated in the top panel) appear noisy due to intensity fluctuations caused by the turbulent flow. Both interferograms are peak normalized, and the pixel 2 interferogram is vertically offset by 0.3 units and horizontally offset by 0.05 cm. *Bottom-right panel*: The real (black) and imaginary (gray) parts of the uncalibrated raw spectrum for both pixel 1 and 2. Both spectra are peak normalized, and the pixel 2 spectrum is vertically offset by 0.5 units. Imaginary parts of the spectra are vertically offset from the real parts by 0.1 units.

the flow field. This source "noise" will result in artifacts in the spectral data and will be discussed in the following section. The corresponding raw spectra $I(\tilde{\nu})$ associated with these interferograms are shown in the bottom-right panel of Figure 4. The spectra are peak-normalized and pixel 2's spectrum has been vertically offset to improve visualization. The real part of the spectrum is shown in black and the imaginary component is shown in gray. The raw spectra for both pixels appear extremely noisy. By comparing the magnitude of the imaginary component of the spectrum to the real part, it can be seen that the apparent signal-to-noise ratio (SNR) is on the order of 1. The scene-change artifacts appear as "noise" and do not appear to differ from actual white noise. However, analysis of the imaginary component of the spectrum has not been performed, and the statistical properties of this apparent noise have not been characterized.

To aid interpreting the "noisy" Telops spectra, Figure 5 displays the spectrum collected by the non-imaging ABB-Bomem FTS. This spectrum represents the temporal average of 4000 individual scans over a FOV encompassing the entire plume with the spectral resolution degraded to match the Telops instrument. The spatially-averaged spectrum cannot be

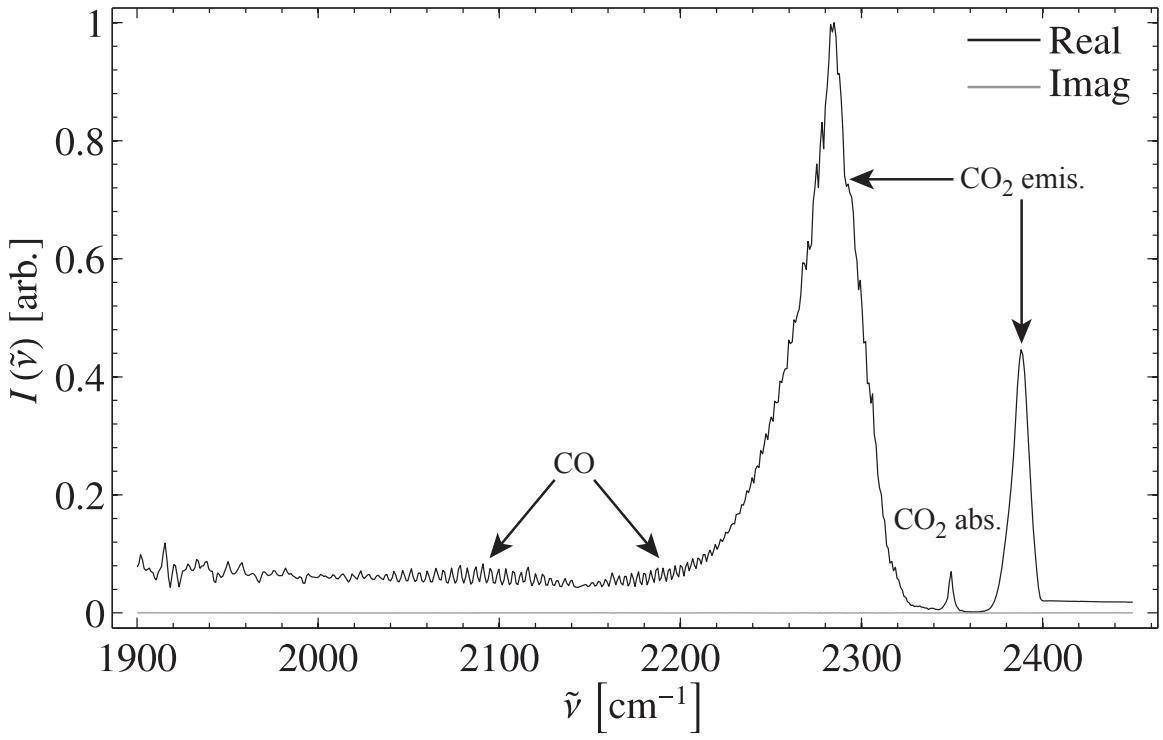

Fig. 5. Average of 4000 spectra of the SR-30 exhaust plume from the non-imaging ABB-Bomem FTS. CO_2 and CO emission features are indicated in the plot.

properly compared with the single-pixel spectrum from the Telops IFTS. However, a qualitative comparison of features aids the interpretation of the Telops spectra. The imaginary part of the ABB-Bomem spectrum is small on this scale, indicating a high SNR. The most prominent feature is emission from CO_2 corresponding to the asymmetric stretching vibrational mode. This same vibrational mode is also responsible for the strong absorption centered at ~2350 cm^{-1} from atmospheric CO_2 along the 11 m path between the plume and instrument. As a consequence of the much higher temperatures in the plume, however, emission in the wings of the absorption feature are easily observed as indicated in the figure. CO rovibrational lines are also evident and correspond to the fundamental ($v = 1 \rightarrow v = 0$) vibrational transition centered at 2143 cm^{-1}. The same CO_2 emission features can be recognized in the Telops spectra for pixel 1 in Figure 4, but noise associated with SCAs prevent spectral identification of CO. It is worth noting that the noise associated with the spectrum would preclude any useful quantitative interpretation. Regarding the pixel 2 spectrum, nothing notable can be observed apart from the broadband background radiation appearing roughly like a linear ramp in intensity with decreasing wavenumber.

To reduce noise associated with SCAs in the Telops data, the 200 interferogram cubes collected in time were averaged. This yielded a significant improvement in the apparent SNR of both the interferograms and the corresponding spectra. Figure 6 presents a summary view of the result of this averaging in the same format as in Figure 4. The top panel represents the average image at the first OPD over the 200 observations. The crop factor, data normalization, and color scale are identical to that used in Figure 4. The average plume intensity features smooth gradations and evidence of the turbulent vortices is absent on this color scale. The difference between the average images at the first and second OPD is shown in the middle panel. The spatial variations in brightness suggest that the effects of turbulence have not been completely averaged away. Note however, that the magnitude of the brightness variations have been reduced considerably as the color scale covers a range ten times smaller than that in the corresponding image in Figure 4.

The temporal averaging substantially reduces the "noise" in the interferograms. The wings of the interferogram ($|x| \gg 0$) are much smaller in comparison to the centerburst ($x \approx 0$), which is expected when examining a source with emission from a broad range of frequencies of light. The corresponding spectra for both pixels 1 and 2, while still "noisy," now contain clear spectral signatures for both CO_2 and CO. Absorption lines due to atmospheric water between 1800–1900 cm^{-1} are

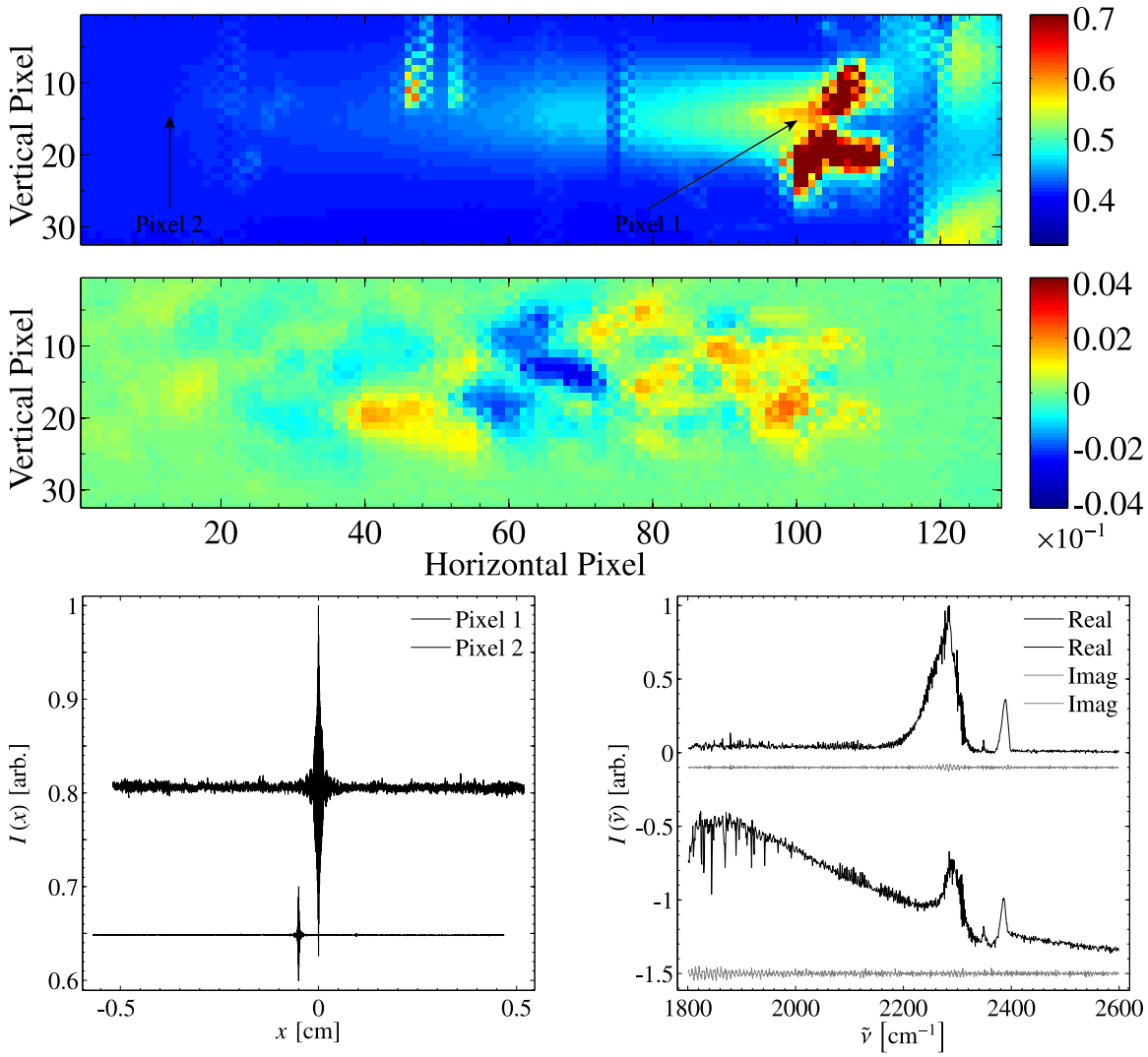

Fig 6. *Top panel*: Broadband image of the turbojet plume at the first OPD after averaging it images at the same OPD across the 200 observations. *Middle panel*: Difference between the first and second averaged broadband images. The color axis covers a range of values that is one order of magnitude smaller than shown in the corresponding plot in Figure 4. *Bottom-left panel*: Interferograms for pixel 1 and 2 corresponding to the average of 200 independent measurements. Both interferograms are peak normalized, and the pixel 2 interferogram is vertically offset by 0.3 units and horizontally offset by 0.05 cm. *Bottom-right panel*: The real (black) and imaginary (gray) parts of the raw average spectrum for both pixel 1 and 2. Both spectra are peak normalized, and the pixel 2 spectrum is vertically offset by 0.5 units. Imaginary parts of the spectra are vertically offset from the real parts by 0.1 units.

also evident in the averaged spectrum. The standard deviation of the imaginary component of the spectrum for pixel 1 was reduced by nearly 11 times upon averaging. By comparison, if the turbulent fluctuations could be treated as a normally-distributed noise term, averaging 200 spectra together would reduce this by $200^{1/2} \approx 14$.

A moderate amount of temporal averaging results in spectra with recognizable molecular emission features. These features reveal information about the plume conditions such as temperature and concentration, and their spatial variation can be used to understand aspects of the steady-state flow field. A particularly striking example of this is presented in Figure 7 which shows temporally-averaged spectra from an earlier measurement campaign using the Telops IFTS against the SR-30 engine. Approximately 100 spectra were collected at a spectral resolution of 16 cm^{-1}. The spectral region is cropped to provide a detailed look at the CO_2 emission feature at several locations down the length of the plume. The average spectra are peak-normalized so that differences in the spectral shape are evident. The width of the emission feature is related to

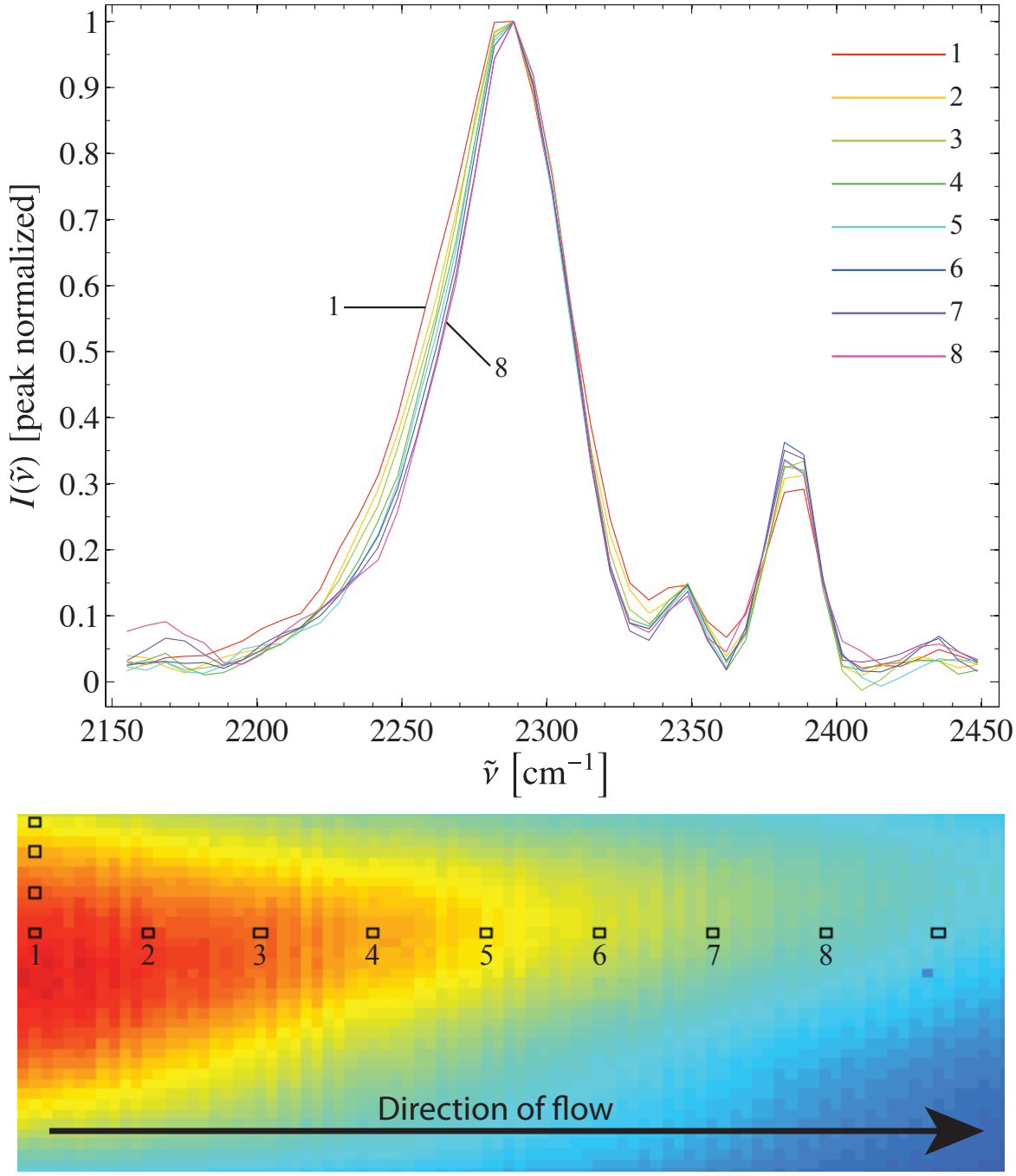

Fig. 7. Temporally-averaged, peak-normalized spectra corresponding to different regions of the engine exhaust plume. The width of the CO_2 emission band decreases with distance from the engine. The width of this spectral feature is related to the temperature of CO_2 and indicates (as expected) that the gas cools as it moves down stream.

the (rotational) temperature of CO_2, with the width of the profile increasing with temperature. The expected decrease in temperature as the gas flows downstream is clearly evident in the shape of the CO_2 emission profile. Both Figures 6 and 7 demonstrate that temporally averaged spectra can be used to study the exhaust plume from a turbojet engine using an IFTS with a small IFOV. Significant information content is present in the spatially-resolved spectra. However, quantitatively interpreting these time-averaged spectra requires an understanding of the effect of stochastic intensity fluctuations on FTS-based measurements, and this issue is briefly discussed in the next section.

4. DISCUSSION

Turbulence in the exhaust flow field causes rapid fluctuations in emitted radiance. This is a consequence of fluctuations in both the density and temperature of the gas. An increase in either density or temperature increases the number of emitting molecular species in a given location. To quantitatively understand radiant plume emissions, the effects of turbulence on the collection of spectra by IFTS, as well as the effects of temporal averaging, need to be further investigated. To this end, a highly simplified model is presented to gain a qualitative understanding of turbulence effects on the intensity measured by a FTS. The model incorporates a series of simplifications to help understand the problem, the first being that the plume is in local thermodynamic equilibrium. Inelastic collision rates are assumed sufficient to ensure a Boltzmann distribution of the rotational and vibrational energy levels at the gas kinetic temperature T. The plume is also assumed to be an optically thin medium such that stimulated emission and self absorption along a line-of-sight (LOS) can be ignored. Finally, assuming background radiation and atmospheric self-emission are negligible, the radiation intensity I along a line of sight through the plume can be expressed at an instant in time t as

$$I(\tilde{\nu}, t) = \tau(\tilde{\nu}) \int \sum_{i,j} \xi_i(l,t)\, N\left(\mathrm{T}(l,t)\right) P_i\left(\tilde{\nu}_j, \mathrm{T}(l,t)\right) A_i\left(\tilde{\nu}_j\right) f_i\left(\tilde{\nu}, \tilde{\nu}_j\right) \mathrm{d}l \tag{1}$$

where τ accounts for atmospheric attenuation between the plume and instrument, ξ_i is fraction of the total number density N for molecule i, P_i is the fraction of molecule i in the excited state defined by the energy $\tilde{\nu}_j$, T is the local instantaneous temperature, $A_{i,j}$ is the Einstein coefficient for spontaneous emission defining the strength of the $\tilde{\nu}_j$ transition in molecule i, and f is the spectral lineshape associated with the transition. The sum accounts for all emission lines j from each molecule i at a specific position l along the LOS through the plume. The integral accounts for contributions to the total intensity along the entire LOS. Since a Boltzmann distribution has been assumed, P_i can be written as

$$P(\tilde{\nu}_j, T) = \frac{g_j \exp\left(-\frac{h c \tilde{\nu}_j}{k_B \mathrm{T}}\right)}{Q} \tag{2}$$

where the g_j denotes the degeneracy of the upper state, h is Planck's constant, c is the speed of light, and k_B is Boltzmann's constant. The total partition function is denoted by Q. The total number density N is expected to behave as an ideal gas as the plume exits the high-temperature, high-pressure environment of the engine.

Predicting the behavior of T and ξ_i at a given location along the LOS at a specific time is a difficult challenge belonging to the domain of reactive-flow computational fluid dynamics. While a detailed understanding of T and ξ_i is not considered in this work, it can be safely assumed that both exhibit stochastic fluctuations about their mean values ‹T› and ‹ξ_i›. Within this simple framework, source intensity fluctuations are driven by the stochastic nature of ξ_i and T. Note that if T is constant at all points l and at all times t, then the intensity of a given molecular emission line would be linearly proportional to the total concentration integrated along the path $\xi_i(t) = \int \xi_i(l,t)\, \mathrm{d}l$. Moreover, while the absolute line intensities change, the relative intensities of emission lines associated with molecule i are preserved. However, if T fluctuates, the population distribution among internal states changes according to Eq. 3, altering the relative line heights in the spectral emission profile. In general, the spectrum integrated along the LOS and averaged in time will be different than that given by Eq. 1 in which T and ξ_i are replaced by their average values, i.e. $\langle I(\tilde{\nu}, \xi_i(t), \mathrm{T}(t))\rangle \neq I(\tilde{\nu}, \langle\xi_i\rangle, \langle\mathrm{T}\rangle)$.

Using this simplified model for a turbulent plume, an interferogram $I(x)$ measured by an ideal FTS at OPD position x_k can be expressed as[1]

$$2I(x_k) = \int_0^\infty I\left(\tilde{\nu}, t = x_k/v\right)\left(1 + \cos(2\pi x_k \tilde{\nu})\right) \mathrm{d}\tilde{\nu} \tag{3}$$

where v is the velocity of the moving mirror, and the spectral intensity I appearing inside the integral is given by Eq. 1. The factor of two appearing on the left hand side accounts for half of the radiation that is either reflected from or transmitted through the beam splitter back out of the instrument. Eq. 3 can be rewritten in terms of the temporally averaged plume intensity $\langle I(\tilde{\nu})\rangle$ and the instantaneous fluctuations about this average intensity:

$$2I(x) = \int_0^\infty \langle I(\tilde{\nu})\rangle\big(1 + \cos(2\pi x\tilde{\nu})\big)\,\mathrm{d}\tilde{\nu} + \int_0^\infty \big(I(\tilde{\nu}, t) - \langle I(\tilde{\nu})\rangle\big)\big(1 + \cos(2\pi x\tilde{\nu})\big)\,\mathrm{d}\tilde{\nu} \quad (4)$$

The last term on the right-hand side captures the instantaneous fluctuations in intensity due to stochastic changes in mole fractions ξ_i and temperature T, and is responsible for the appearance of "noise" in the interferograms. The second integral can be made small in the limit that a large number of interferograms are averaged. In this case, the mean spectrum $\langle I(\tilde{\nu})\rangle$ can be obtained by a Fourier transform. The timescale of the fluctuations dictates the number of interferograms that need to be averaged. For example, if the timescale associated with the turbulent fluctuations is large compared to the time between measurements at x_k and x_{k+1} (but small compared to the total measurement timescale), then a large number of interferograms will need to be collected in order to recover the interferogram of the mean spectral intensity $\langle I(\tilde{\nu})\rangle$. To reduce the number of interferograms that need to be collected, the measurement time at x_k needs to be longer than the characteristic timescale associated with the turbulent fluctuations. One way of achieving this is by employing a step-scanning collection mode. At each OPD, a large number of broadband images would be collected and averaged so that a steady-state plume image would be formed. Alternatively, a reduction of the optical throughput via neutral density filters or a small aperture stop could be implemented so that an FPA integration time exceeding the turbulence timescale could be chosen.

A proper understanding of the exhaust plume phenomenology will aid in the development of a simple model to quantitatively interpret the spectra. Bowen performed the first step in interpreting the spectra obtained from the SR-30 turbojet[19]. Lacking *a priori* information about the temperature and density fluctuations in the plume, he proceeded to model the spectra with the assumptions that $\langle I(\tilde{\nu}, \xi_i(t), T(t))\rangle = I(\tilde{\nu}, \langle\xi_i\rangle, \langle T\rangle)$ and that a single temperature was sufficient to describe the LOS-integrated spectra. His model was fit to the spectrum at each pixel to obtain spatial maps of temperature, H_2O, CO and CO_2 concentrations. The agreement between the spectra and the model was surprisingly good; however, for many pixels the fit residuals were larger than the noise and exhibited spectrally structured patterns particularly in the CO_2 emission region between 2250–2350 cm^{-1}. Additionally, the fitted temperatures differed from the thermocouple readings by approximately 200 K. These systematic errors are not surprising considering the simplicity of the model, and it is likely that they can be reduced by accounting for LOS temperature variations and turbulent effects on the observed average spectra. Schäfer *et al*. use a more sophisticated radiative transfer model which takes into account temperature gradients and the effects of emission and self-absorption along the LOS.[11] They report a systematic biasing in the spectrally-estimated temperatures and concentrations from the exhaust spectra. It is worth noting that the effects of turbulence were not taken into account. However, turbulent effects can produce large instantaneous variations in temperature, which will have substantial effects on the radiation field.[20]

5. CONCLUSIONS

Measurements of a turbulent exhaust plume have been made with an imaging Fourier-transform spectrometer. Despite the large variations in scene intensity, useful information can be extracted from the data through moderate temporal averaging. Scene-change artifacts associated with the turbulence translate into high-frequency "noise" in the spectra and can be reduced via temporal averaging to reveal spatial maps of temperature and various exhaust concentrations. An accurate, quantitative model for these spatially-resolved, temporally-averaged spectra requires an understanding of the temperature and density distributions in the plume flow field. Such a model would make it possible to benchmark computational fluid dynamic simulations of turbulent flow fields from jet engines with measured data that is unprecedented in terms of simultaneous high-spatial and high-spectral resolutions.

REFERENCES

[1] Bell, R.J. Introduction to Fourier Transform Spectroscopy, Academic Press. New York, NY, 1972.
[2] Davis, S.P.; Abrams, M.C.; Brault, J.W. Fourier Transform Spectrometry. Academic Press, San Diego, CA, 2001.
[3] Dlug, D.D.; Whalley, E. "Effects of source noise in Fourier-transform spectroscopy," Journal of the Optical Society of America, 64 (7), 1019–1020 (1974).
[4] Kick, H.; Tank, V.; Lindermeir, E. "Impact of scene changes during data acquisition in Fourier spectroscopy," Journal of Quantitative Spectroscopy and Radiative Transfer, 92, 447–455 (2005).

[5] Mitchell, H.J.; Hemmer, T.H.; Lewis, P.E.; Salvaggio, C. “The effects of temporally changing sources on Fourier transform spectrometers,” Proc. SPIE 4381, 516–526 (2001).
[6] Orson, J.A.; Bagby, W.F.; Perram, G.P. “Infrared signatures from bomb detonations.” Infrared Physics & Technology, 44 (2), 101–108 (2003).
[7] Gross, K.C.; Wayman, J.; Perram, G.P. “Phenomenological fireball model for remote identification of high explosives.” Proc. SPIE 6566, 656613 (2007).
[8] Gross, K.C. “Phenomenological model for infrared emissions from high-explosive detonation fireballs.” Ph.D. Dissertation, AFIT/DS/ENP/07-03, Air Force Institute of Technology, 2007.
[9] Gross, K.C.; Perram, G.P. “The phenomenology of high explosive fireballs from fielded spectroscopic and imaging sensors for event classification.” International Journal of High Speed Electronics & Systems, 18 (1), 19–29 (2008).
[10] Heland, J.; Schäfer, K. “Analysis of aircraft exhausts with Fourier-transform infrared emission spectroscopy.” Applied Optics 36 (21), 4922–4931 (1997).
[11] Schäfer, K; *et al*. “Nonintrusive optical measurements of aircraft engine exhaust emissions and comparison with standard intrusive techniques.” Applied Optics 39 (3), 441–455 (2000).
[12] Arrigone, G.; Hilton, M. “Theory and practice in using Fourier transform infrared spectroscopy to detect hydrocarbons in emissions from gas turbine engines.” Fuel 84, 1052–1058 (2005).
[13] Rusch, P. *et al*. “SIGIS HR: A system for measurement of aircraft exhaust gas under normal operating conditions of an airport.” Proc. SPIE 5979, 597922 (2005).
[14] Flores-Jardines, E. *et al*. “Investigation of temperature and gas concentration distributions in hot exhausts (airplanes and burners) by scanning imaging FTIR spectrometry.” Proc. SPIE 5979, 59791A (2005).
[15] Dubois, P. *et al*. “FPGA SoC architecture for imaging FTS real-time data processing,” Optical Society of America, p. JWA9 (2007).
[16] Vallières, A. *et al*., “Algorithms For Chemical Detection, Identification And Quantification For Thermal Hyperspectral Imagers,” Proc. SPIE Vol. 5995, p. 147-157 (2005).
[17] Farley, V. *et al*., “Chemical Agent Detection and Identification with a Hyperspectral Imaging Infrared Sensor,” Proc. SPIE Vol. 6661 (2007).
[18] Turbine Technologies, http://www.turbinetechnologies.com.
[19] Bowen, S. “Hyperspectral imaging of a turbine engine exhaust plume to determine radiance, temperature, and concentration spatial distributions.” MS Thesis, AFIT/GAP/ENP/09-M02 (2009).
[20] Modest, M.F. “Multiscale modeling of turbulence, radiation, and combustion interactions in turbulent flames.” International Journal for Multiscale Computational Engineering, 3, 85–106 (2005).